UNIVERSITY OF LEEDS

This is a repository copy of *Monolithic Patch-Antenna THz Lasers with Extremely Low Beam Divergence and Polarization Control*.

White Rose Research Online URL for this paper:
https://eprints.whiterose.ac.uk/171392/

Version: Supplemental Material

**Article:**
Pérez-Urquizo, J, Todorov, Y, Li, L orcid.org/0000-0003-4998-7259 et al. (5 more authors) (2021) Monolithic Patch-Antenna THz Lasers with Extremely Low Beam Divergence and Polarization Control. ACS Photonics, 8 (2). pp. 412-417. ISSN 2330-4022

https://doi.org/10.1021/acsphotonics.0c01430

© 2021 American Chemical Society. This is an author produced version of an article published in ACS Photonics. Uploaded in accordance with the publisher's self-archiving policy.

**Reuse**
Items deposited in White Rose Research Online are protected by copyright, with all rights reserved unless indicated otherwise. They may be downloaded and/or printed for private study, or other acts as permitted by national copyright laws. The publisher or other rights holders may allow further reproduction and re-use of the full text version. This is indicated by the licence information on the White Rose Research Online record for the item.

**Takedown**
If you consider content in White Rose Research Online to be in breach of UK law, please notify us by emailing eprints@whiterose.ac.uk including the URL of the record and the reason for the withdrawal request.

White Rose university consortium
Universities of Leeds, Sheffield & York

eprints@whiterose.ac.uk
https://eprints.whiterose.ac.uk/

# Supporting Information. Monolithic patch-antenna THz lasers with extremely low beam divergence and polarization control: supplemental document.

Joel Pérez-Urquizo,[1] Yanko Todorov,[2] Lianhe Li,[3] Alexander G. Davies,[3] Edmund H. Linfield,[3] Carlo Sirtori,[2] Julien Madéo,[1,*] and Keshav M. Dani[1].

[1]Femtosecond Spectroscopy Unit, Okinawa Institute of Science and Technology Graduate University, Onna-son, Okinawa 904-0495, Japan.

[2]Laboratoire de Physique de l'Ecole normale supérieure, ENS, Université PSL, CNRS, Sorbonne Université, Université de Paris, F-75005 Paris, France.

[3]School of Electronic and Electrical Engineering, University of Leeds, Leeds, LS2 9JT, United Kingdom.

List of Figures:

Figure S1 … … … … … … … … … … … … … … … … … … … … … … … … … … … … …..S2

Figure S2 … … … … … … … … … … … … … … … … … … … … … … … … … … … … …..S3

Figure S3 … … … … … … … … … … … … … … … … … … … … … … … … … … … … …..S3

Figure S4 … … … … … … … … … … … … … … … … … … … … … … … … … … … … …..S4

Figure S5 … … … … … … … … … … … … … … … … … … … … … … … … … … … … …..S6

Figure S6 … … … … … … … … … … … … … … … … … … … … … … … … … … … … …..S7

Figure S7 … … … … … … … … … … … … … … … … … … … … … … … … … … … … …..S8

Figure S8 … … … … … … … … … … … … … … … … … … … … … … … … … … … … …..S9

## Note 1

### L-I-V characteristics

Here we show the L-I-V characteristics for the three devices exhibiting different polarization states presented in Fig. 4. All measurements were taken in pulsed mode at a temperature of 77 K. A wired-grid analyzer was set in between a Golay cell detector and the cryostat containing the devices. The Golay cell was calibrated using a Thomas Keating absolute power meter. Red and blue curves display the THz output power for two cross-polarized signals. Fig. S1 exhibits the characteristics for the device emitting with a linear polarization (*s*= 12 μm, *d*= 40 μm). Maximum emission occurs in the direction parallel to the interconnecting wires. Fig. S2 shows the measurements relative to the device with an elliptical polarization (*s*= 16 μm, *d*= 15 μm). In this case, the signal polarized perpendicular to the wires' direction is slightly larger than the emission along the wires for all the lasing operation. An elliptical polarization with the semi-major axis oriented perpendicular to the wires is then observed in Fig. 4 (b). Finally, Fig. S3 corresponds to the circularly polarized array (*s*= 15 μm, *d*= 25 μm), where the cross-polarized emissions are of equal magnitude at all injection currents.

All the devices showed similar current density threshold and display different output power and dynamic ranges which is a direct consequence of the losses due to the specific configurations and in particular the relative contribution between radiative and ohmic losses (see Note 6).

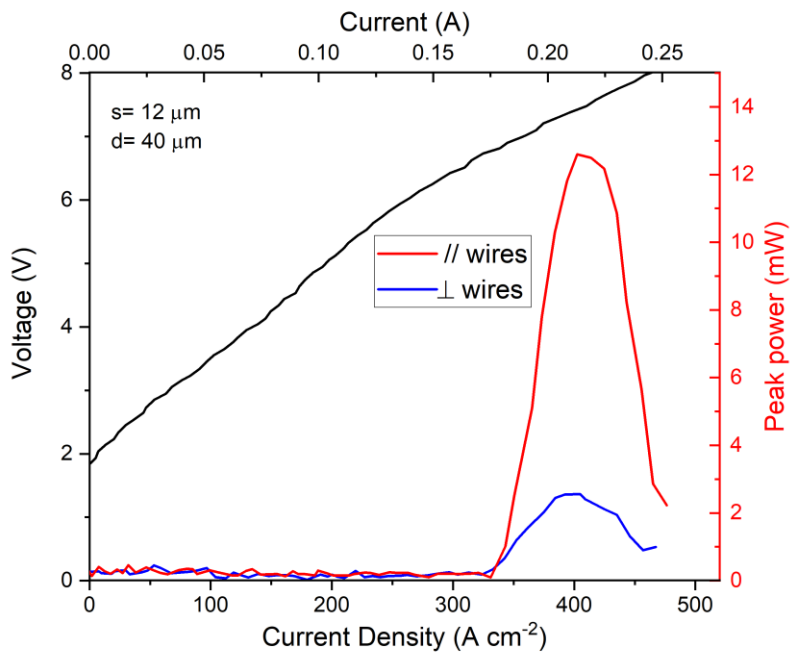


Figure S1. Pulsed L-I-V characteristics (50 kHz, 25% duty cycle) of a device with patch sizes s=12 μm and wires of length d=40 μm, measured at 77 K. The THz peak power of two cross-polarized signals are shown in red (polarization parallel to the wires) and blue (polarization perpendicular to the wires).

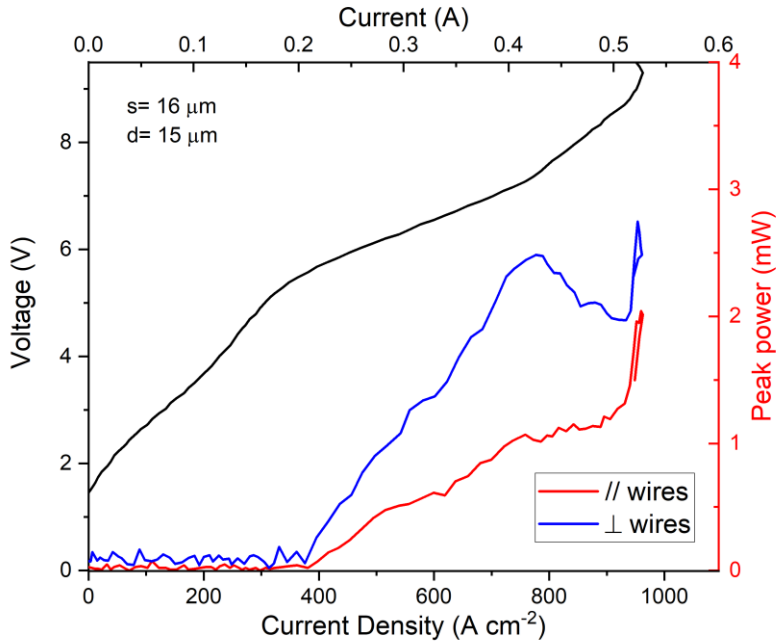


Figure S2. Pulsed L-I-V characteristics (50 kHz, 25% duty cycle) of a device with patch sizes s=16 μm and wires of length d=15 μm, measured at 77 K. The THz peak power of two cross-polarized signals are shown in red (polarization parallel to the wires) and blue (polarization perpendicular to the wires).

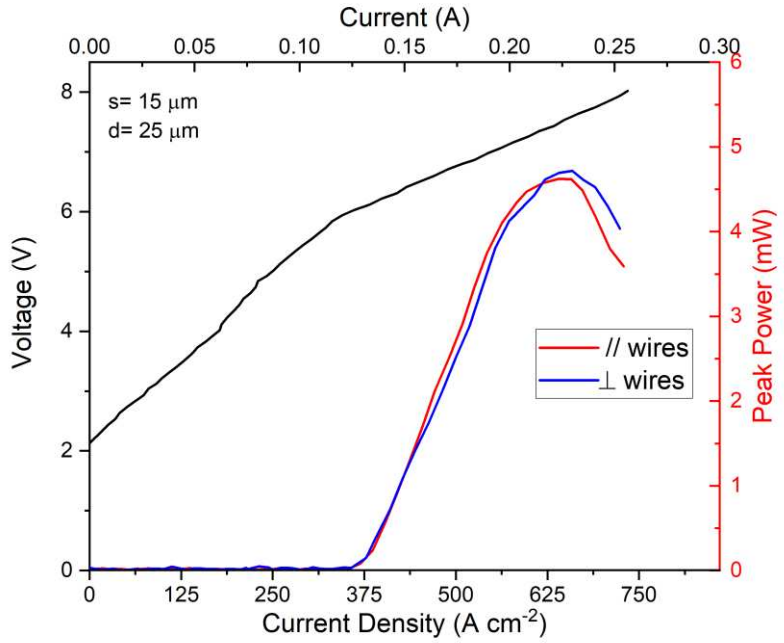


Figure S3. Pulsed L-I-V characteristics (10 kHz, 25% duty cycle) of a device with patch sizes s=15 μm and wires of length d=25 μm, measured at 77 K. The THz peak power of two cross-polarized signals are shown in red (polarization parallel to the wires) and blue (polarization perpendicular to the wires).

## L-I-V characteristics of a double metal ridge waveguide.

To compare the performance of our devices with a conventional structure, we processed a device into a standard double metal ridge waveguide (100 μm-wide, 1.5 mm long). Fig. S4 shows the L-I-V characteristics of the ridge waveguide and a patch microcavity array (only L-I) with parameters $s$=15 μm, $d$= 40 μm. Data was acquired in pulsed mode operation (50 kHz, 10% duty cycle) at a heat-sink temperature of 10 K. Maximum peak power reaches 19 mW with a threshold current density $J_{ot}$=238 A/cm$^2$ (25 mW output power and $J_{ot}$=270 A/cm$^2$ for the patch microcavity array). To compare the performance between the patch array and the ridge waveguide laser, we calculated the power delivered per unit of electrically pumped area ($P_A$) for both devices. For the ridge, we calculated $P_A$= 0.08 W·mm$^{-2}$, whereas a $P_A$= 0.4 W·mm$^{-2}$ was obtained for the patch microcavity array corresponding to a 5-fold better performance of the patch microcavity device compared to the conventional ridge waveguide laser.

In the inset of Fig. S4, we show the multimode spectrum from the ridge waveguide device. The Fabry-Perot laser emits on high-order lateral modes over a bandwidth of 400 GHz. To compare the relative resonant frequencies of the patch modes as seen in Fig.4 (d), (e) and (f), we assume this quantity to be close to the QCL active region spectral gain which is in the range what has been previously reported for bound-to-continuum and LO-phonon depopulation designs using Time-Domain Spectroscopy [1, 2].

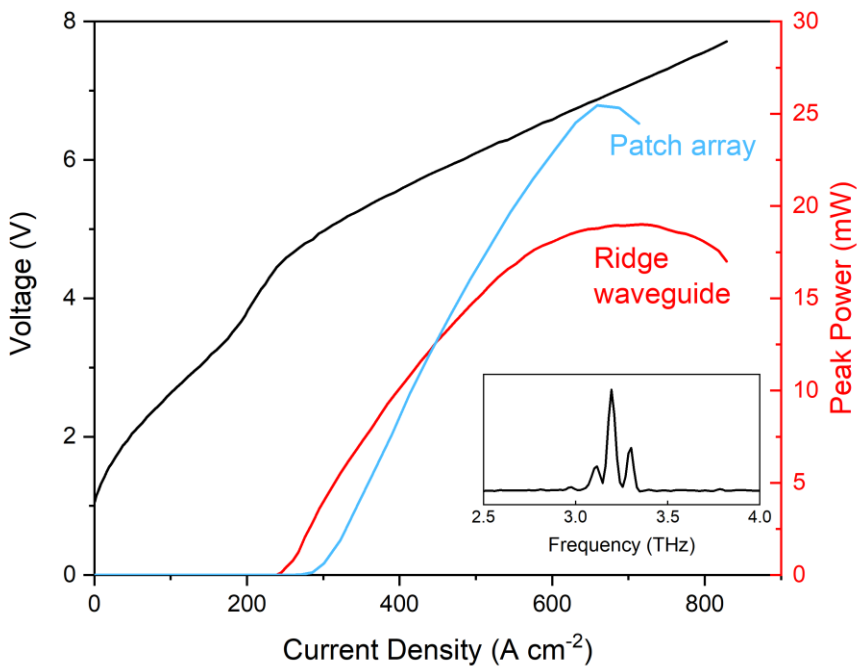


Figure S4. Pulsed L-I-V characteristics (50 kHz, 10% duty cycle) of a double metal ridge waveguide (100 μm-wide, 1.5 mm long) and L-I characteristics (light blue) of a patch microcavity array (s=15 μm, d= 40 μm). Inset: THz spectrum of the ridge waveguide QCL.

## Note 2

## Antenna Theory

In the RF and microwave bands, arrays of antennas are used to produce directive patterns by tailoring the emission of individual antennas in the far-field, so that constructive and destructive interferences occur in specific directions. This is achieved by controlling different parameters: the geometrical configuration of the array, the number of

antenna elements in the array, the spacing between antennas and the excitation amplitude and phase of individual elements. Given that our devices are based on patch antennas, the same analysis used in conventional microwave antenna theory can be used to understand the basic trend of the beam shaping from our microcavity structures. Considering a planar array formed by positioning individual antennas along a square grid, and assuming the same excitation (both magnitude and phase) for all the elements, the angular distribution of the total emitted power in the far-field can be approximated by [3] :

$$P_{tot}(\theta,\varphi) = P_0(\theta,\varphi)\left|\frac{1}{N^2}\frac{\sin\left(\frac{N}{2}\psi_x\right)}{\sin\left(\frac{\psi_x}{2}\right)}\frac{\sin\left(\frac{N}{2}\psi_y\right)}{\sin\left(\frac{\psi_y}{2}\right)}\right|^2$$

Where $\psi_x = kd_x \sin\theta\cos\varphi$ and $\psi_y = kd_y \sin\theta\sin\varphi$.

Here, $P_0$ corresponds to the power emitted from a single antenna element. The term following this quantity is known as the array factor, and it contains the dependence of the far-field emitted power on the array parameters, where N is the number of resonators aligned in the x- and y- direction, and $\boldsymbol{d_x}$, $\boldsymbol{d_y}$ are the spatial antenna periodicities in x- and y- directions, respectively. This simple model allows to intuitively understand the general trends and the influence of array parameters on the far-field. We used the array factor expression to investigate the main trend of the far-field pattern emitted by a planar array of antennas emitting at 3.2 THz (λ=94 μm). Fig. S5 shows the calculated FWHM divergence angles for various arrays containing different number of elements N along the x- and y- direction (N=2,4,6,8 and 10) as a function of the separation distance between individual elements. The curves were extracted along the constant plane θ= 0 from the 2D array factor term. The FWHM divergence angle shows a monotonic decrease with the separation distance between elements, but as the number of elements N increases, a saturation of the divergence angle occurs. This trend is in agreement with our FEM simulations shown in Fig. 3 (d). We observe an asymptotic decay of the FWHM divergence angles with $N^2$, i.e. the parameter N dictates essentially the beam width for a 10x10 array. Experimentally, we observed no influence of the periodicity on the FWHM divergence for arrays of 10x10 elements, as noted in Fig. 4.

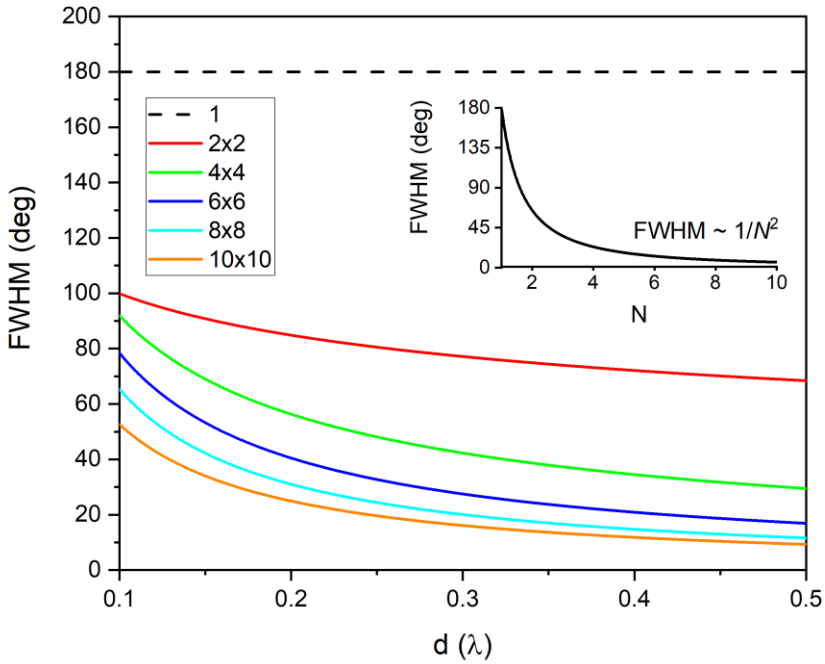


Figure S5. FWHM divergence angles as a function of the separation distance between antennas calculated from the array factor term for planar arrays containing NxN elements (where N=2,4,6,8 and 10). Dashed line represents the single element isotropic case. Inset: FWHM as a function of the numbers of elements for an array with elements distanced by a half wave.

## Note 3

## Side lobes in the far-field pattern

In Fig.S6, we show the presence of low intensity side lobes in the far-field pattern. This is a direct result of the beam formation by the constructive interference and a very general result of antenna arrays. For a planar array of NxN identical antenna elements separated by a distance *dx* and *dy* in the *x*- and *y*- direction respectively, the far-field radiation pattern can be approximated by the *array factor AF*:

$$AF(\theta,\varphi) = \left| \frac{1}{N^2} \frac{\sin\left(\frac{N}{2}\psi_x\right)}{\sin\left(\frac{\psi_x}{2}\right)} \frac{\sin\left(\frac{N}{2}\psi_y\right)}{\sin\left(\frac{\psi_y}{2}\right)} \right|^2$$

Where $\psi_x = kd_x \sin\theta \cos\varphi$ and $\psi_y = kd_y \sin\theta \sin\varphi$. This expression determines the distribution of the energy radiated by the antenna array in the far-field. Due to its periodic nature, local maxima appear on the entire domain of the space coordinates. Thus, the appearance of side lobes (local maxima) is a direct consequence of arraying antennas. In our measurements, we observe two lateral lobes, located are around 5 ° and 10 ° from the main lobe (see Fig. S6). In our simulations, we also observe the presence of side lobes with an order of magnitude lower intensity, in agreement with our measurement.

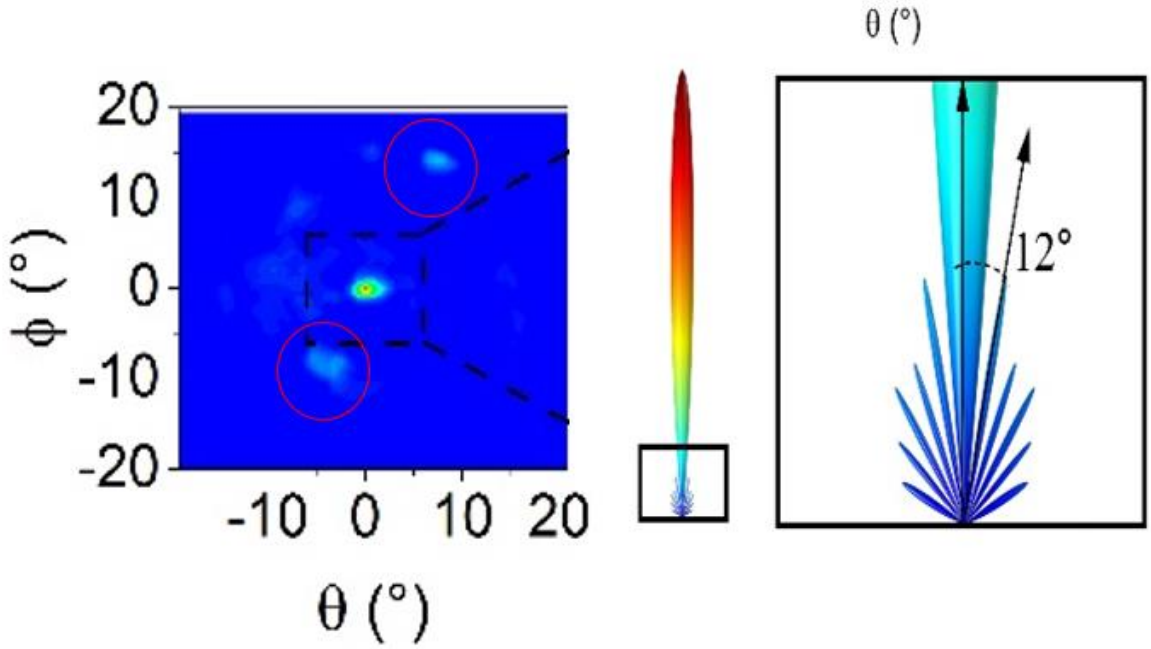


Figure S6. Left panel: Identification of lateral lobes (circled in red) in the measured far-field pattern. Right panel: 3D far-field pattern obtained by the simulations. A close-up view of the secondary lobes is shown in the black square to indicate the direction of the first lateral lobe.

## Note 4

## Far-field pattern for extended arrays

In principle, it is possible to design arrays with a larger area and a larger number of resonators in order to obtain an even narrower far-field emission. The crucial element that defines the beam shaping in our devices is the aperture size of the device, which can be defined as the electrical area that the radiator utilizes to emit electromagnetic waves (i.e., $N \times N \cdot s^2$) [3, 4]. The relation between the emitted electric field pattern in the far field and the aperture distribution is given by the spatial-frequency two-dimensional Fourier transformation (Fraunhofer diffraction principle). Then, if the aperture of the device is of infinite extent, the radiation pattern would take the form of a Dirac delta in the direction of the main lobe. The limiting factor for achieving usable devices is rather practical. Figure S7 shows a simulation of the FWHM divergence for finite antenna arrays. The beam divergence shows an asymptotic behavior following a $\sim 1/N^2$ dependence.

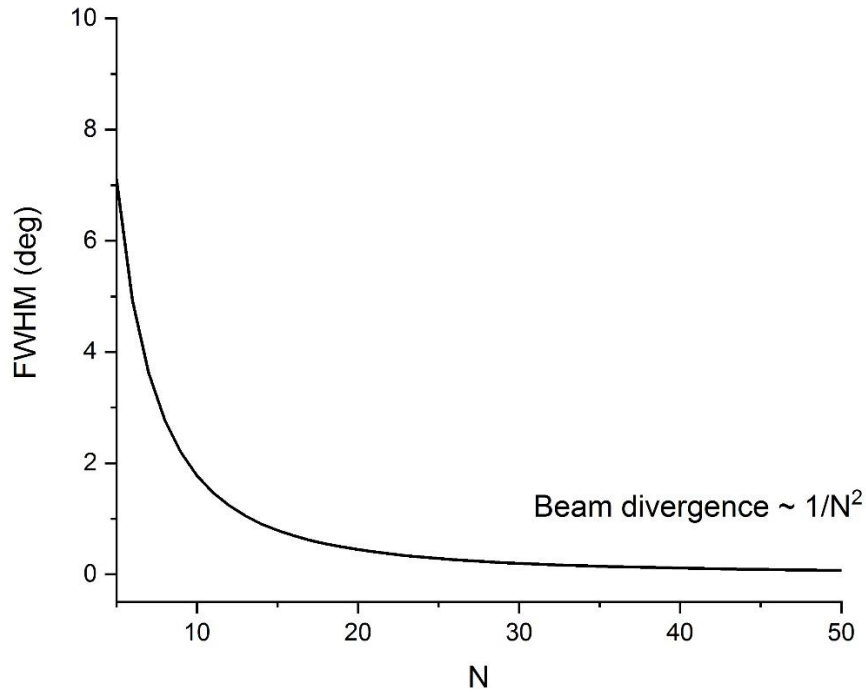


Figure S7. Simulated FWHM divergence as a function of *N*.

In practice, we found that an array consisting of 10x10 antenna elements delivered good electrical and optical characteristics while providing an excellent beam quality. In principle, one could increase the number of resonators, however this could come with a higher probability of meeting lithographic errors and would also require a higher power current supply and possibly larger cryogenic consumption.

## Note 5

## Coherence of the polarization states.

In the RF range, coherent control of the polarization from arrays of antennas has been extensively studied[5]. In particular, for patch antennas, it has been shown that the fringing fields located at the corners of the patch extend in the orthogonal direction[6] providing a non-zero cross-polarized contribution[7, 8] and allowing to mutually couple orthogonal modes in the array. This results in the phase-locking of the $TM_{01}$ and $TM_{10}$ modes and their associated coherent superposition.

To demonstrate that our arrays emit with coherent polarized states, a quartz quarter waveplate was placed in between the wire-grid analyzer and the Golay cell detector. As shown in Fig.S8, we were able to convert a quasi-circular polarized beam (DOCP= 98%) into a linearly polarized signal. This would be impossible in the case of a superposition of incoherent polarization states.

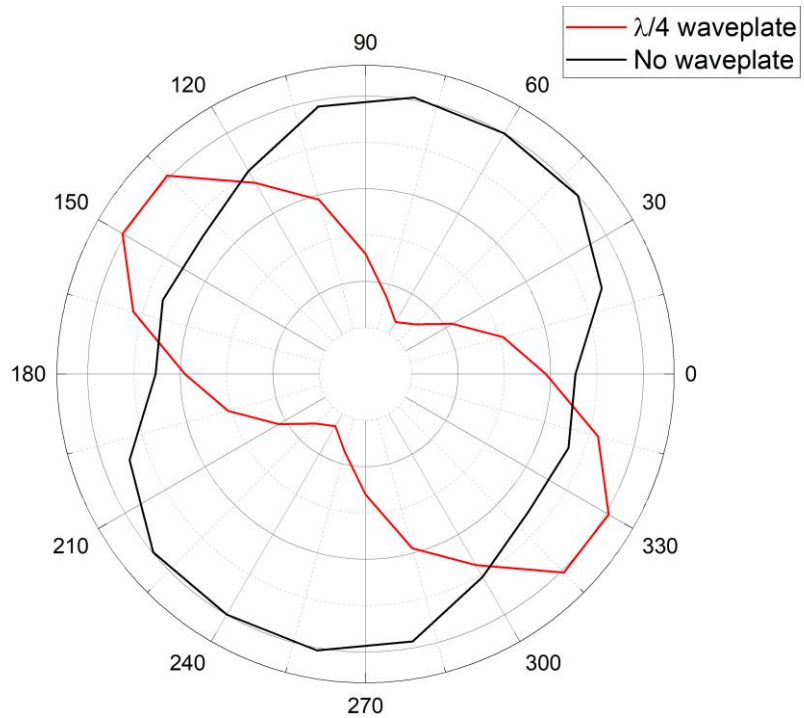

Figure S8. Polar plot of the polarization state from a coherent beam (black), and a linearly polarized signal (red) obtained by placing a quarter waveplate in between the wire-grid polarizer and detector.

## Note 6

## Quality factors and photon extraction efficiency

As shown in Fig.S3, it is possible to have an emission of equal magnitude from the orthogonal contributions, although the Q factor of $TM_{10}$ is much lower than $TM_{01}$. The output power does not depend directly on the Q factor but more precisely to the radiative losses of the resonator. In general, the Q factor is composed of a radiative and non-radiative contribution such that:

$$\frac{1}{Q} = \frac{1}{Q_{rad}} + \frac{1}{Q_{nr}}$$

Where $Q_{rad}$ and $Q_{nr}$ correspond to the radiative and non-radiative Q factors. Here, the non-radiative contribution accounts for ohmic and dielectric losses.

The relevant quantity to consider is the photon extraction efficiency, defined as:

$$\eta = \frac{Q}{Q_{rad}}$$

This quantity directly provides the ratio of photons that can escape the resonator. We have performed simulations in a similar manner as in Ref 9 to extract both contributions in the total Q factor. In the case of a circular polarization, for which $TM_{10}$ and $TM_{01}$ emit with the same magnitude, we find that $\eta = 0.77$ for the $TM_{10}$ and 0.71 for the $TM_{01}$. In this case, we then expect the magnitude of both contributions to be similar. When considering photon extraction efficiencies, the $TM_{01}$ mode has a higher Q factor but its $Q_{rad}$ contribution is lower than the $Q_{rad}$ contribution to the

Q factor of the $TM_{10}$ mode. This is due to the presence of the wires that provide a stronger confinement for the $TM_{01}$ mode which lowers the radiative losses.

Regarding the device presented in Fig.S2, we also calculate a similar extraction efficiency for the two modes. Here, the polarization state is elliptical as the phase difference set by the separation between resonators is different than $\pi/2$. Additionally, the magnitude of the ellipticity can be tuned by adjusting the patch size which detunes the mode resonant frequency with respect to the radiative electronic transition. The detuning impacts directly the output power as previously described in Ref 10 in the case of a single mode laser.

## References


1. Jukam, N.; Dhillon, S. S.; Oustinov, D.; Zhao, Z.-Y.; Hameau, S.; Tignon, J.; Barbieri, S.; Vasanelli, A.; Filloux, P.; Sirtori, C.; Marcadet, X., Investigation of spectral gain narrowing in quantum cascade lasers using terahertz time domain spectroscopy. *Applied Physics Letters* **2008,** *93* (10), 101115.
2. Jukam, N.; Dhillon, S. S.; Oustinov, D.; Madéo, J.; Tignon, J.; Colombelli, R.; Dean, P.; Salih, M.; Khanna, S. P.; Linfield, E. H.; Davies, A. G., Terahertz time domain spectroscopy of phonon-depopulation based quantum cascade lasers. *Applied Physics Letters* **2009,** *94* (25), 251108.
3. Balanis, C. A., *Antenna Theory. Analysis and design.* Fourth Edition ed.; John Wiley & Sons, Inc.: 2016; p 1072.
4. Headland, D.; Monnai, Y.; Abbott, D.; Fumeaux, C.; Withayachumnankul, W., Tutorial: Terahertz beamforming, from concepts to realizations. *APL Photonics* **2018,** 3 (5), 051101.
5. Simeoni, M.; Lager, I. E.; Coman, C. I.; Roederer, A. G., Implementation of polarization agility in planar phased-array antennas by means of interleaved subarrays. *Radio Science* **2009,** *44* (5).
6. Chattopadhyay, S.; Chakraborty, S., A Physical Insight Into the Influence of Dominant Mode of Rectangular Microstrip Antenna on Its Cross-Polarization Characteristics and Its Improvement With T-Shaped Microstrip Antenna. *IEEE Access* **2018,** *6*, 3594-3602.
7. Hansen, R., Cross polarization of microstrip patch antennas. *IEEE Transactions on Antennas and Propagation* **1987,** *35* (6), 731-732.
8. Bhardwaj, S.; Rahmat-Samii, Y., Revisiting the generation of cross-polarization in rectangular patch antennas: A near-field approach. *IEEE Antennas and Propagation Magazine* **2014,** *56* (1), 14-38.
9. Madéo, J.; Pérez-Urquizo, J.; Todorov, Y.; Sirtori, C.; Dani, K. M., Engineering the Losses and Beam Divergence in Arrays of Patch Antenna Microcavities for Terahertz Sources. *Journal of Infrared, Millimeter, and Terahertz Waves* **2017,** *38* (11), 1321-1330.
10. Mehendale, S. C., Dependence of laser intensity on cavity losses for a detuned, single-mode laser. *Appl. Opt.* **1994,** *33* (36), 8330-8332.